



This is a repository copy of *p-Type/n-type behaviour and functional properties of K_xNa(1-x)NbO₃ (0.49 ≤ x ≤ 0.51) sintered in air and N₂*.

White Rose Research Online URL for this paper:

<http://eprints.whiterose.ac.uk/129467/>

Version: Accepted Version

Article:

Hussain, F., Sterianou, I., Khesro, A. et al. (2 more authors) (2018) p-Type/n-type behaviour and functional properties of K_xNa(1-x)NbO₃ (0.49 ≤ x ≤ 0.51) sintered in air and N₂. Journal of the European Ceramic Society, 38 (9). pp. 3118-3126. ISSN 0955-2219

<https://doi.org/10.1016/j.jeurceramsoc.2018.03.013>

Reuse

Items deposited in White Rose Research Online are protected by copyright, with all rights reserved unless indicated otherwise. They may be downloaded and/or printed for private study, or other acts as permitted by national copyright laws. The publisher or other rights holders may allow further reproduction and re-use of the full text version. This is indicated by the licence information on the White Rose Research Online record for the item.

Takedown

If you consider content in White Rose Research Online to be in breach of UK law, please notify us by emailing eprints@whiterose.ac.uk including the URL of the record and the reason for the withdrawal request.

p-type/n-type behaviour and functional properties of $K_xNa_{(1-x)}NbO_3$ ($0.49 \leq x \leq 0.51$) sintered in air and N_2

Fayaz Hussain^{\$+}, Iasmi Sterianou^{*}, Amir Khesro^{\$x}, Derek C. Sinclair^{\$} and Ian. M. Reaney^{\$}

**\$ Department of Material Science and Engineering, University of Sheffield, Mappin St,
Sheffield, S1 3JD, UK**

*** Department of Engineering and Mathematics, Materials Engineering, Sheffield Hallam
University, Sheffield, S1 1WB, UK**

**+Materials Engineering, NED University of Engineering & Technology, Karachi, 75270,
Pakistan, Corresponding Author: fhussain@neduet.edu.pk Mobile: +92-333-3946604**

x Department of Physics, Abdul Wali Khan University, Mardan, Pakistan

Abstract

Potassium sodium niobate (KNN) is a potential candidate to replace lead zirconate titanate in sensor and actuator applications but there are many fundamental science and materials processing issues to be understood before it can be used commercially, including the influence of composition and processing atmosphere on the conduction mechanisms and functional properties. Consequently, KNN pellets with different K/Na ratios were sintered to 95% relative density in air and N_2 using a conventional mixed oxide route. Oxygen vacancies ($V_O^{••}$) played a major role in the semi-conduction mechanism in low $p(O_2)$ for all compositions. Impedance spectroscopy and thermo-power data confirmed KNN to be n-type in low $p(O_2)$ in contradiction to previous reports of p-type behaviour. The best piezoelectric properties were observed for air-sintered samples with $d_{33}=125$ pC/N and $k_p=0.38$ obtained for $K_{0.51}Na_{0.49}NbO_3$.

Keywords: p-type, n-type, low $p(O_2)$, oxygen vacancies, Seebeck coefficient

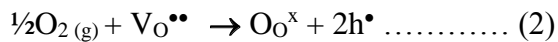
Introduction

Piezoelectric ceramics are an important class of functional materials but the majority are based on $\text{Pb}(\text{Zr},\text{Ti})\text{O}_3$ (PZT) which may be subject to future legislation as part of the European Directives, Restriction of Hazardous Substances (ROHS) and Waste Electrical and Electronic Equipment (WEEE) because of the toxicity of Pb. Hence, there is extensive research in academia and industry to find suitable lead-free piezoelectrics to replace PZT. $\text{K}_{0.5}\text{Na}_{0.5}\text{NbO}_3$ (KNN) and $\text{Na}_{0.5}\text{Bi}_{0.5}\text{TiO}_3$ based compositions are currently the leading contenders. The former is compatible with cheap Ni-based internal electrodes [1] and it is therefore feasible to manufacture low cost KNN multilayer devices but there are significant doubts over the environmental credentials of KNN due to the deleterious impact of Nb mining [2]. KNN-based ceramics are however, non-toxic with respect to PZT and thus may be used within the human body for micromotor and sensing applications. [3,4].

Despite its potential importance, there are only a few studies of KNN processed under reducing conditions. Fisher et al. (2009) sintered KNN under a range of $\text{p(O}_2)$ and noted that the polymorphic transition temperatures ($T_{\text{O-T}}$ & $T_{\text{T-C}}$) decreased as a function of decreasing $\text{p(O}_2)$ with similar phenomena reported by Glaister et al (1960), DeVries (1960), Hardtl et al (1972) and Lee et al. (2007) for BaTiO_3 [5-8]. In each case, the decrease in Curie temperature (T_C) was attributed to the loss of lattice oxygen with the formation of oxygen vacancies ($\text{V}_{\text{O}}^{\bullet\bullet}$). Nb^{5+} is a d^0 cation and can therefore accommodate the electrons associated with oxygen loss. Consequently, KNN has the potential to be an n-type semiconductor in inert and reducing conditions, as described by the defect equation:



Supporting evidence for this proposition may be found in the work of Kobayashi et al. (2012) who reported that Li substituted on the B-site in KNN acts as an acceptor and consequently reduced KNN-LiF has a much higher resistivity than equivalent air-sintered ceramics. [9]. However, many other authors have claimed KNN exhibits p-type behaviour induced by volatilisation of alkali oxides during processing. [10, 11] This facilitates the uptake of oxygen into the lattice via the $\text{V}_{\text{O}}^{\bullet\bullet}$ formed after the volatilisation of the alkali oxides, according to the equation



If KNN is to replace PZT, dopant strategies are required which can modify its properties in a manner similar to that adopted for ‘hard’ and ‘soft’ piezoelectrics. The controversy in the scientific literature over whether KNN exhibits p or n-type behaviour has for many years inhibited research into the development of such dopant strategies. The aim of this paper therefore, is to establish unambiguously the semiconductor behaviour and functional properties of KNN ceramics as a function of $\text{p(O}_2)$.

Experimental Procedure

Ceramic Processing

Nb_2O_5 (Standford Materials Corporation 99.999%), Na_2CO_3 (Aldrich, 99.5%) and K_2CO_3 (Fisher Scientific, 99.5%) raw materials were selected for the study. After drying the carbonates at 300 °C and oxides at 900 °C for 24 hours, 30g batches of $(\text{K}_x\text{Na}_{1-x})\text{NbO}_3$ $0.49 \leq x \leq 0.51$ (KNN-100x/100(1-x)) were weighed using appropriate proportions. Batches of KNN were attrition milled for 1h in a 500 ml jar at 300 rpm in isopropanol using 3mm diameter Y_2O_3 stabilised ZrO_2

media prior to calcination. After milling, the slurry was washed with isopropanol, separated from the milling media through a sieve and dried at 80 °C for 24 hours. The dried material was sieved through a 150 µm mesh and calcined 4h at 850 °C at 3 °C/min and 5 °C/min heating and cooling rates, respectively. The calcined powder was re-milled prior to uniaxial pressing (~200 MPa) into 10 mm diameter green pellets and then sintered at different temperatures in air and N₂ atmospheres. Pellet density was measured using the Archimedes' method and compared with the theoretical density based calculated from crystallographic data. All measured pellets achieved > 95 % theoretical density.

Structural and microstructural characterisation

XRD traces of calcined powders and crushed sintered pellets were obtained using a Siemens D500 (or D5000) diffractometer over a 2θ range of 5° - 80° with a scanning speed of 1°/min. and step size 0.05° using CuKα radiation ($\lambda = 1.5418 \text{ \AA}$). To calibrate peak positions and to calculate accurate lattice parameters, Si powder (99% pure, -325 mesh size, Aldrich) was mixed with KNN crushed pellets. A scan range of 2θ = 5°- 80° with step size 0.02° and a speed of 0.1 °/min were selected for more precise analysis. The X-ray powder density was also calculated from the obtained lattice parameters.

For scanning electron microscopy, sintered pellets were ground and polished using SiC papers (800 mesh, 1200 mesh) and 6, 3, 1 µm diamond paste respectively, then cleaned by acetone and thermally etched for 30 minutes at 10 % lower than their respective sintering temperature. Samples were mounted on Al stubs with Ag paste and coated in C. Secondary electron images (20 kV) and EDS analysis were obtained on a JEOL SEM (Model6400, Tokyo, Japan).

Electrical Characterisation

The dielectric properties were measured using an LCR meter (Model4284A, Hewlett Packard). Primary electrodes of Au were pasted on both flat surfaces of the ceramics and fired at 800 °C. Au electrode pellets were then connected between Pt secondary electrodes to form a capacitor. The sample was placed in a non-inductively wound tube furnace, with extra thermocouples near the pellet for accurate temperature measurements. The LCR meter was connected to a computer through a CP-IB interface. Capacitance and $\tan\delta$ were measured from room temperature to 700 °C at 1, 10, 100, and 250 kHz and 1MHz. Capacitance values were converted to relative permittivity, ϵ_r , according to equation (3):

$$\epsilon_r = \frac{c}{\epsilon_0} \cdot \frac{t}{A} \quad \dots\dots\dots (3)$$

where, c = capacitance, ϵ_0 = permittivity of free space ($8.85419 \times 10^{-12} \text{F}\cdot\text{m}^{-1}$), t = thickness of pellet and A = Area of the electrode. Impedance spectroscopy data were collected using a Solartron SI 1260 Impedance/Gain-Phase Analyser from room temperature to 600 °C from 0.01 Hz to 1MHz with AC amplitude of 100 mV. The data were corrected using a sample geometry factor and analysed in Z-View Software.

Thermopower measurements were performed on 20 mm bar samples to calculate the Seebeck coefficient. The samples were placed in a ProboStat™ A (NorECs AS) cell connected to a sensitive digital voltmeter (KEITHLEY 182), and the cell was retracted a few cm from the centre of the hot zone of a tube furnace to establish a thermal gradient. At different temperature gradients (ΔT), the \pm voltage (ΔV) values were measured using a voltmeter.

Polarization versus electric field (P-E) loops (Figure 3-14) were obtained using a ferroelectric tester composed of an RT66A signal generator (Radiant Technology, 70 USA) linked to a high voltage interface (HVI), power box (PB) and a high voltage amplifier (HVA, Trek). Electroded pellets (see section 3.5) were placed in silicone oil between Cu electrodes. The maximum applied field was 90 kV/cm. Poling of the electroded thin disc samples was carried out by using a high voltage power supply (Model PS350 / 5000V – 25W, SRS: Stanford Research Systems, Inc.) at 40kV/cm and at 100°C with a 20 minute hold time, followed by cooling to room temperature under applied voltage. After poling, d_{33} values were measured by a Piezometer (Piezotest PM300, PiezoMeterSystem), operating at a frequency of 110Hz and at dynamic force of 0.25N. No attempt was made to study aging phenomena but samples retained approximately the same value of d_{33} when measured several months later. Poled samples were also tested in the resonant frequency range (Agilent 4295A precision Impedance Analyser) to obtain the piezoelectric electromechanical coupling factor (k_p).

Results and Discussion

XRD traces of crushed KNN pellets calcined/sintered in air and N₂ are shown in Figure 1. All major peaks are indexed according to an orthorhombic KNN structure (ICDD card No. 00-032-0822) with a minor peak attributed to a tetragonal tungsten bronze (TTB) structured phase (K₃Nb_{5.4}O₁₅, ICDD card No 04-010-8978), present in air but not in N₂ sintered samples. After calibrating and correcting the traces of KNN-50/50Air by using an internal Si standard, the lattice parameters, cell volume (V_{cell}) and theoretical density (ρ_{th}) were obtained as a = 5.6510(3) Å, b = 3.9436(11) Å, c = 5.6726(21) Å, V_{cell} = 126.42(6) Å³ and ρ_{th} = 4.51 g/cm³, respectively.

For other ratios and conditions, structural parameters were similar as the compositional changes were marginal within the sample set.

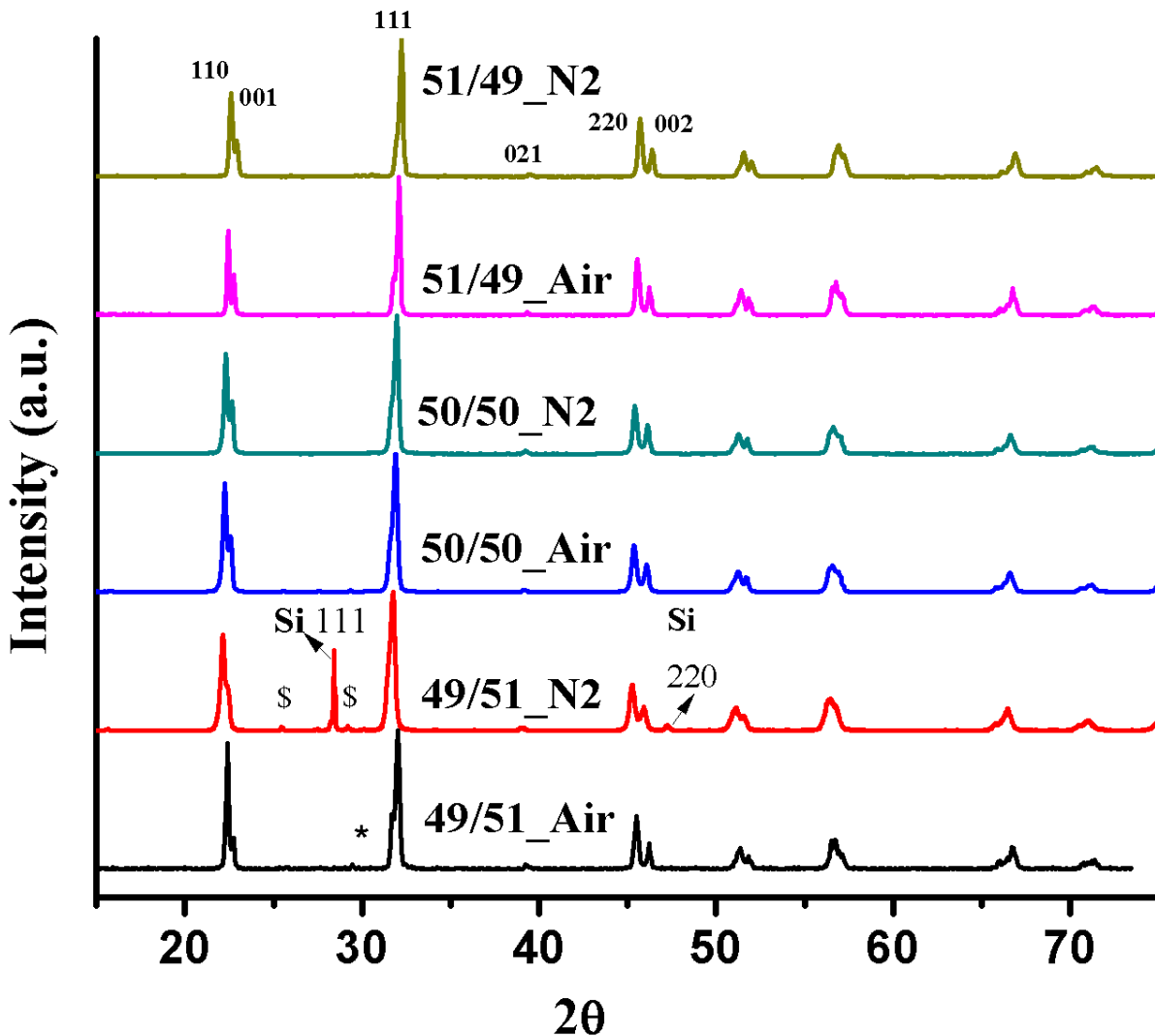


Figure1. XRD patterns from sintered KNN samples, * denotes a peak associated with a tetragonal tungsten bronze phase and $\$$ peaks due to the Si powder used as an internal standard.

NB the numeric label denotes the K/Na ratio and N2 or air the sintering atmosphere

SEM images of fracture surfaces of air and N₂ sintered KNN compositions are consistent with a relative density > 95 %. The grains of KNN are cubic in morphology as commonly reported by

other researchers [12]. In Na-rich samples, a fine grain size was observed ($1\text{-}3\mu\text{m}$) as shown in Figure 2(a), despite this composition (KNN-49/51) being sintered at a slightly higher temperature. In polished and thermally etched samples of air sintered KNN-50/50, some large grains are observed which give rise to qualitatively different EDS spectra than the small grained matrix, Figure 2(b). It is assumed these larger grains correspond to the TTB phase, recorded in the XRD patterns in Figure 1.

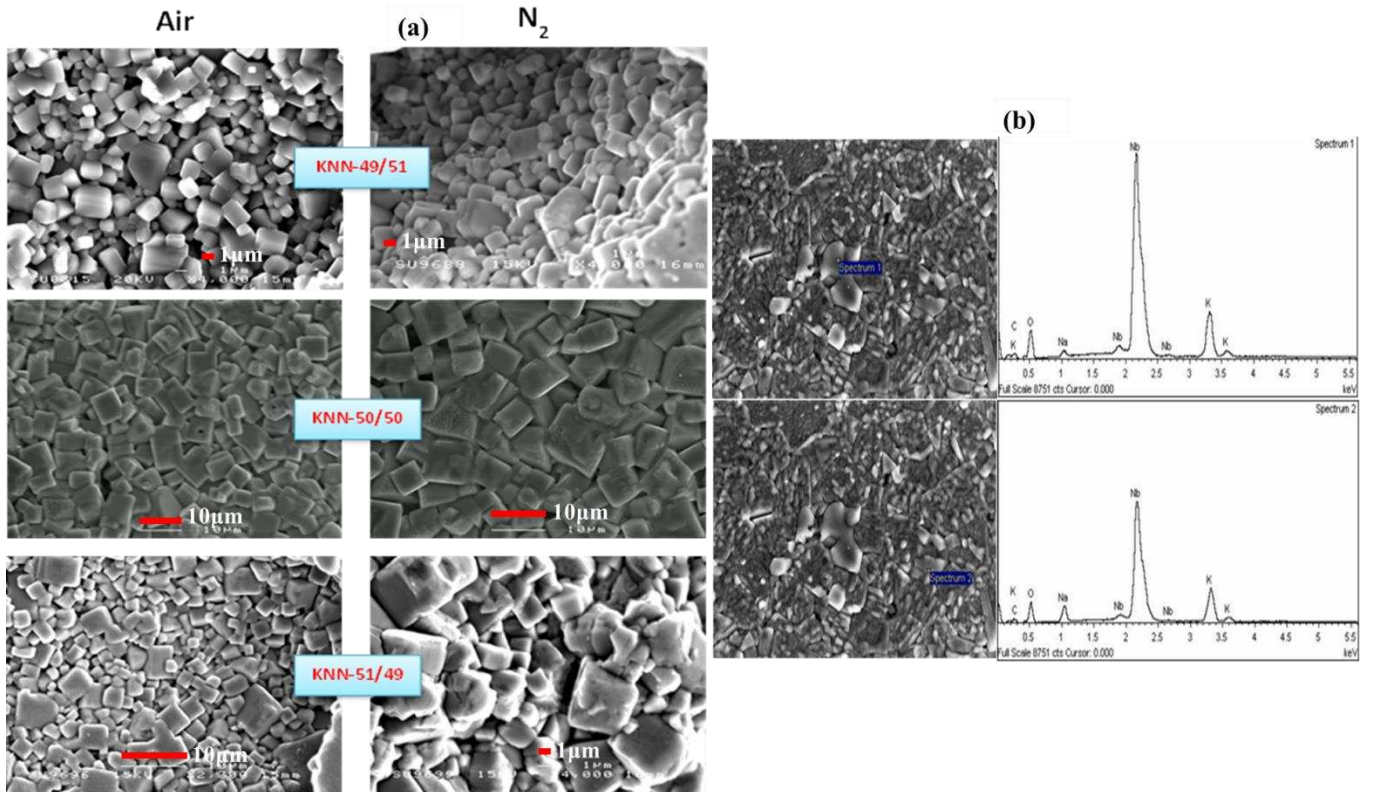


Figure 2. (a) SEM images of fracture surfaces of N_2 and air sintered KNN compositions, (b) EDS spectra of the polished surface of air sintered KNN-50/50.

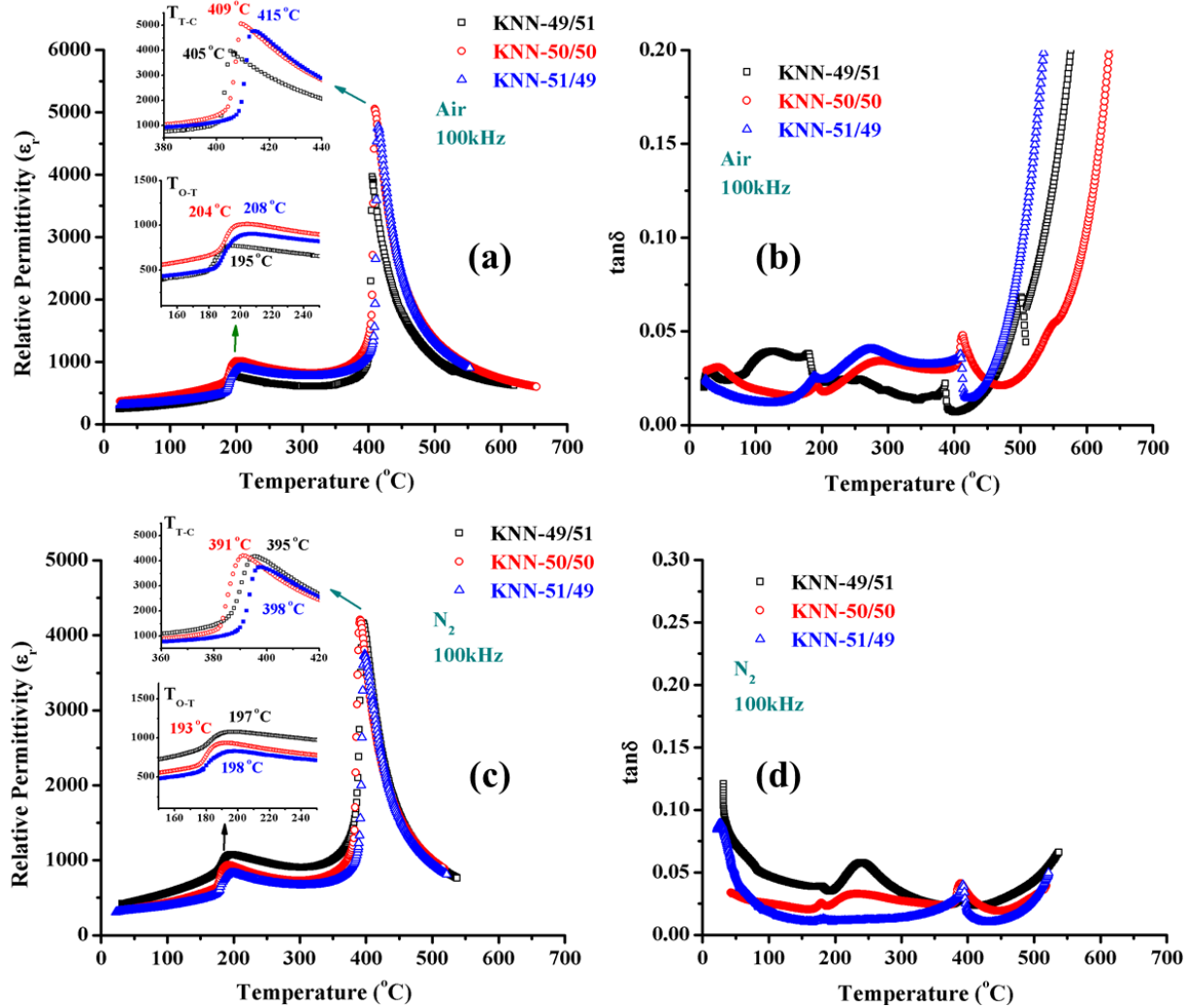


Figure 3. (a & c) Temperature dependence of ϵ_r at 100 kHz of air and N₂ sintered KNN and (b & d) the temperature dependence of $\tan\delta$ at 100 kHz of air and N₂ sintered KNN, and all transition temperatures are shown in the zoomed insets.

Relative permittivity and $\tan\delta$ vs. temperature obtained at 1 MHz for KNN ceramics sintered in air and N₂ are shown in Figure 3. In each sample, two peaks are visible and the transition temperatures T_{O-T} & T_{T-C} are given in the expanded insets, Figure 3(a-c). N₂ sintered consistently show a lower T_{O-T} & T_{T-C} than air-sintered samples with a systematic decrease in T_{O-T} & T_{T-C} as the K/Na ratio decreased in air-sintered samples. However, the compositional ranking order

differs in N₂ sintered samples with KNN-51/49 having the highest and KNN-50/50 the lowest T_{O-T} & T_{T-C}. The decrease in T_C for all compositions may relate to the formation of V_O^{••} during sintering in N₂ as discussed by Fisher (2009) for KNN-50/50 [6] and by DeVries (1960) and Lee et al. (2007) for BaTiO₃. tan δ at room temperature is higher in air/N₂ processed KNN-49/51 and air processed 51/49 formulations as compared to KNN-50/50.

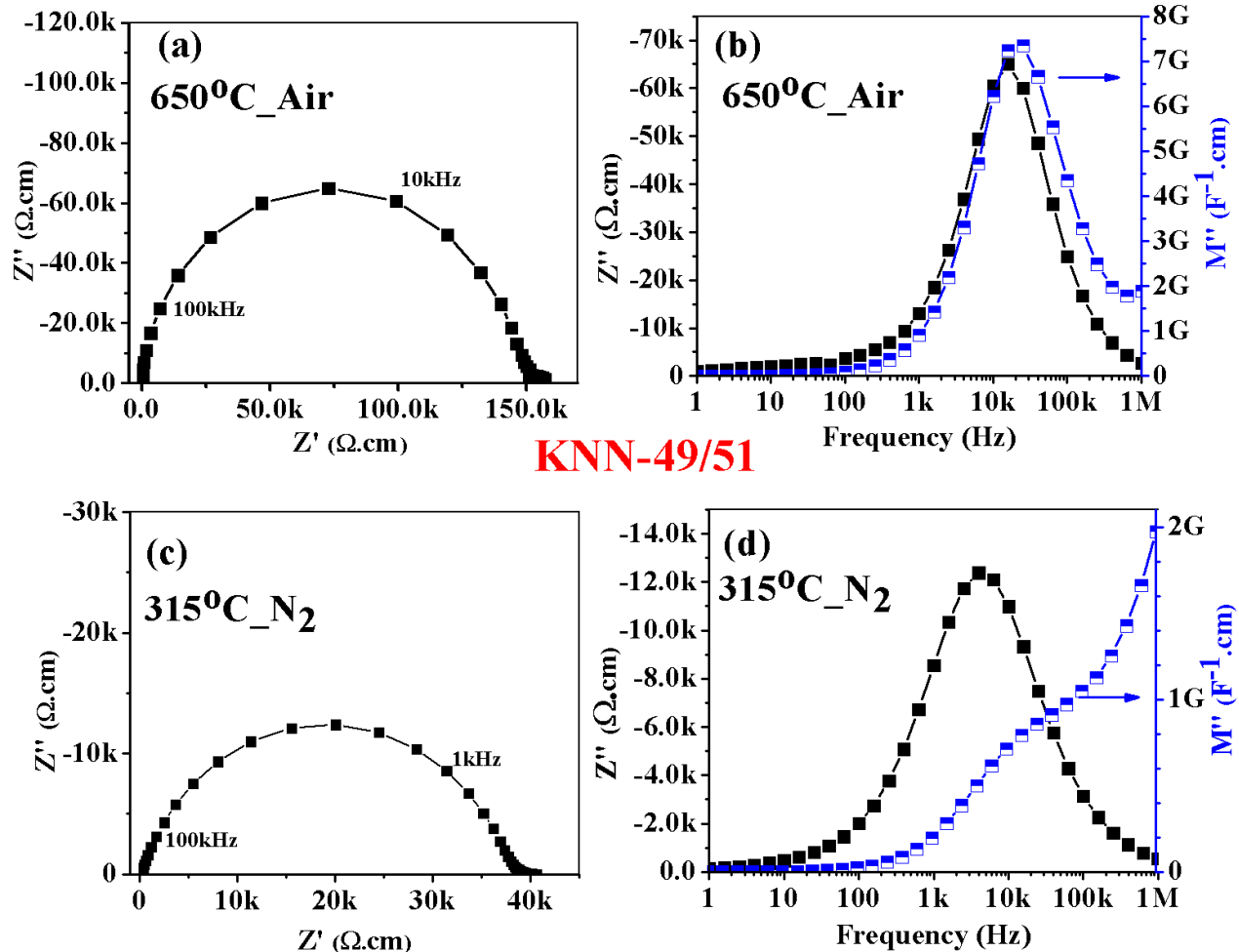


Figure 4. Complex impedance plot (Z^*) and combined spectroscopic plot of M'' and Z'' , of (a-d) KNN-49/51 sintered in air and N₂ over the frequency range 0.1 Hz to 1 MHz.

Figure 4-7 show combined spectroscopic plots of M'' and Z'' and complex Z^* plots of air/N₂ sintered KNN within the frequency range from 0.1 Hz to 1 MHz. All KNN samples except one

(Figure 4(c-d)), exhibit single semicircles with single Debye peaks of combined Z'' and M'' spectroscopic plots as a bulk response (R_bC_b) which indicate that these ceramics have a homogenous electrical microstructure. In contrast, electrical inhomogeneity was observed in the N_2 sintered 49/51 (Na-rich) composition as shown in Figure 4(c) & (d) where a grain boundary resistance is dominant in the Z'' spectrum with the M'' spectrum showing a high frequency incline, indicating that the bulk (grain) response is much more conductive in this sample. This is in agreement with the higher dielectric loss observed for this sample in Figure 3(d). The Z^* plot shows a single semicircle which corresponds to the more resistive grain boundary response in this sample. [13] This response converted to the bulk (grain) when the sample was annealed in air at $650^\circ C$ for one day and again in N_2 for one day, Figure 5(a-d). The bulk (grain) response becomes more conductive in N_2 but still looks dominant because the magnitude of M'' is similar in both air and N_2 annealed samples. Consequently, it is proposed that the inhomogeneity is not associated with any cation compositional change but with V_O^{2+} . In comparison, air annealed samples of KNN-49/51 originally sintered in N_2 Figure 5(a-b) are more resistive than the corresponding air sintered samples Figure 4(a-b).

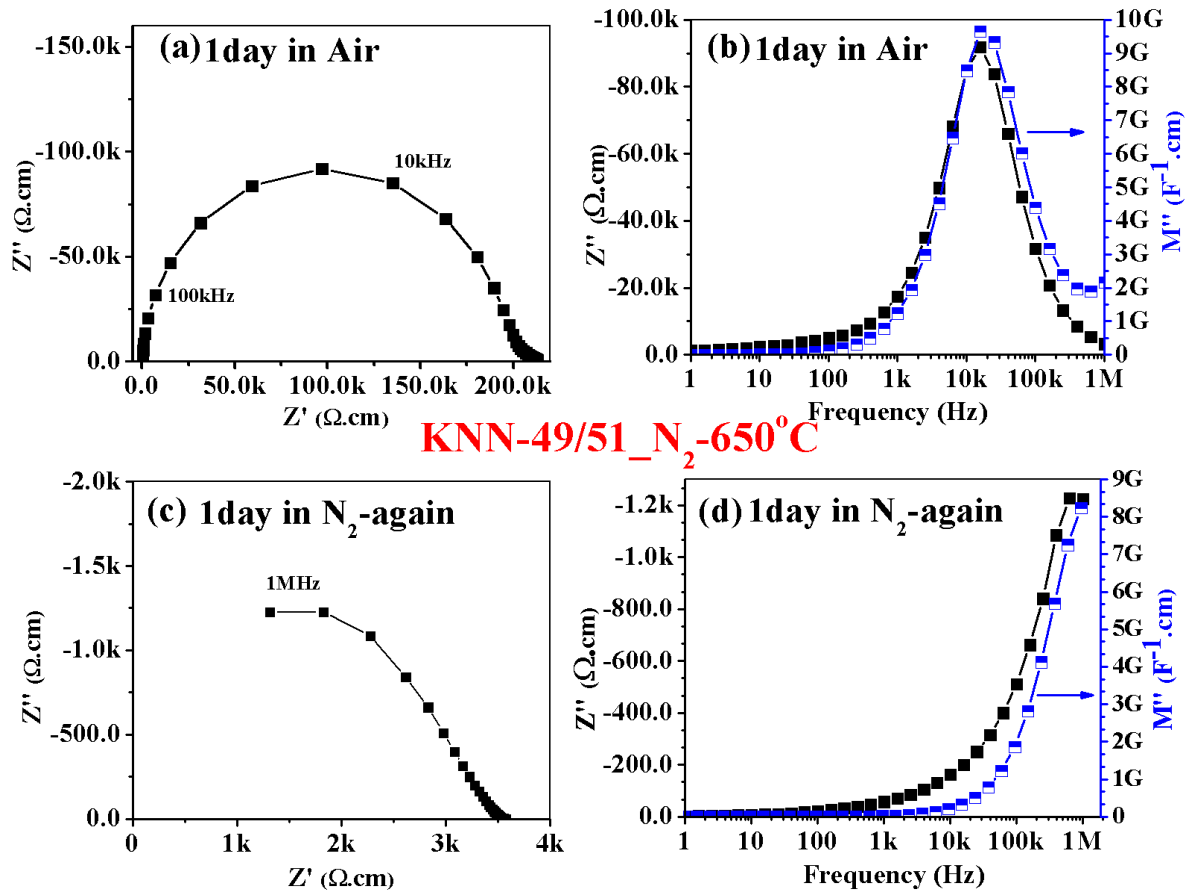


Figure 5. Bulk response after annealing at 650°C in air/N₂ of KNN-49/51 initially **sintered in N₂**.

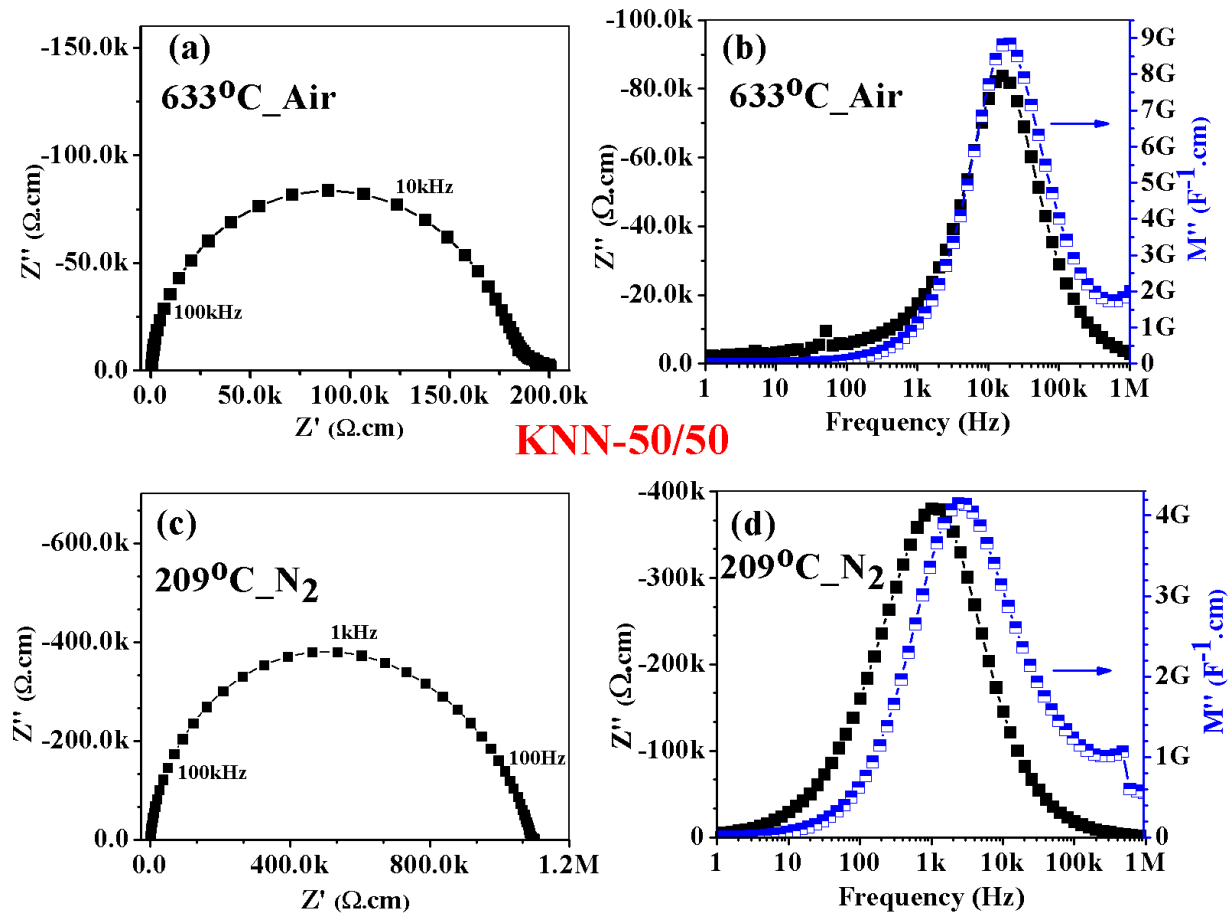


Figure 6. Complex impedance plot (Z^*) and combined plot of M'' and Z'' , of (a-d) KNN-50/50 sintered in air and N_2 over the frequency range 0.1 Hz to 1 MHz.

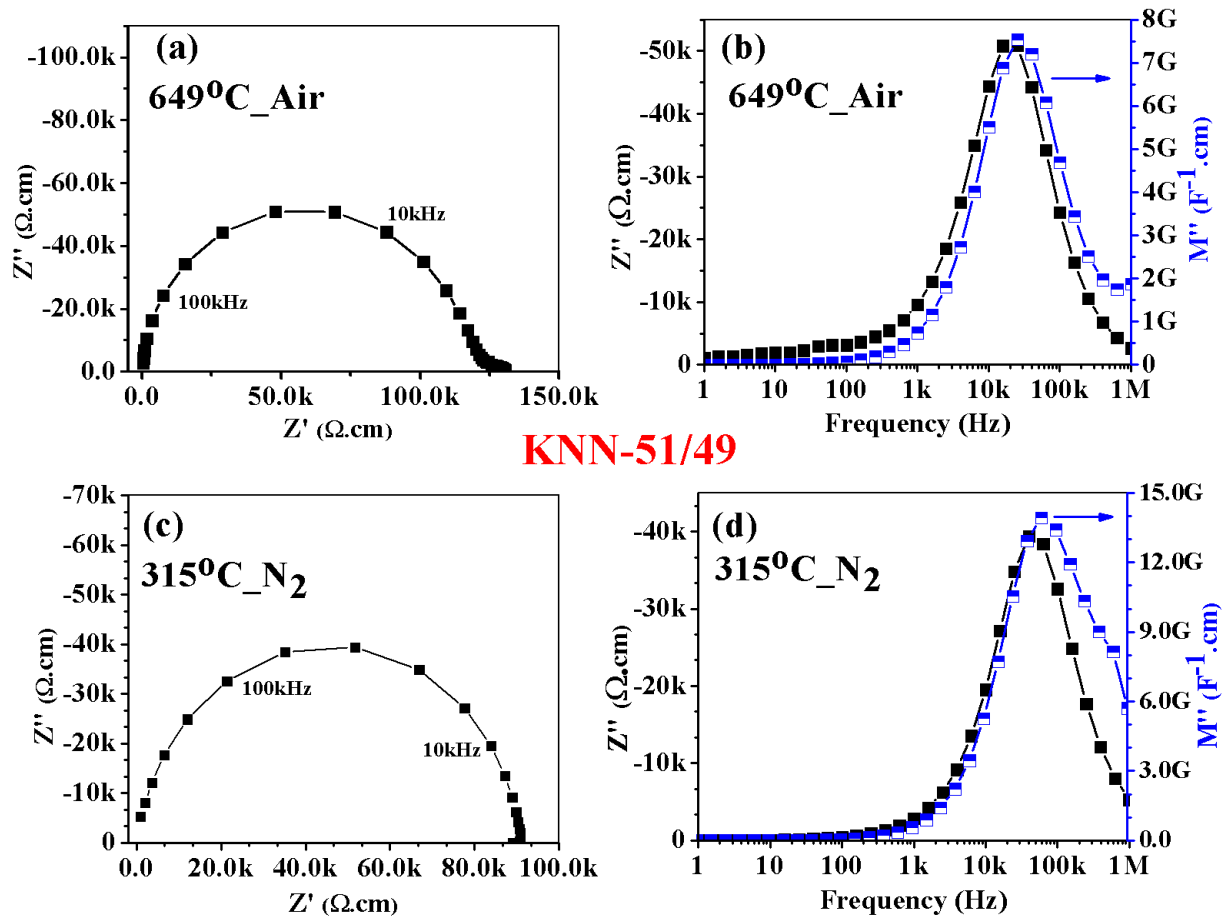


Figure 7. Complex impedance plot (Z^*) and combined spectroscopic plot of M'' and Z'' , of (a-d) KNN-51/49 sintered in air and N_2 , respectively over the frequency range 0.1 Hz to 1 MHz.

Figure 8 shows an Arrhenius plot of bulk conductivity vs. temperature for both air and N_2 sintered pellets, where the data were taken from the low frequency intercept of the Z^* plot. As discussed above the conductivity of air sintered samples is lower and the activation energy for conduction is slightly higher than for the N_2 sintered samples of KNN-50/50.

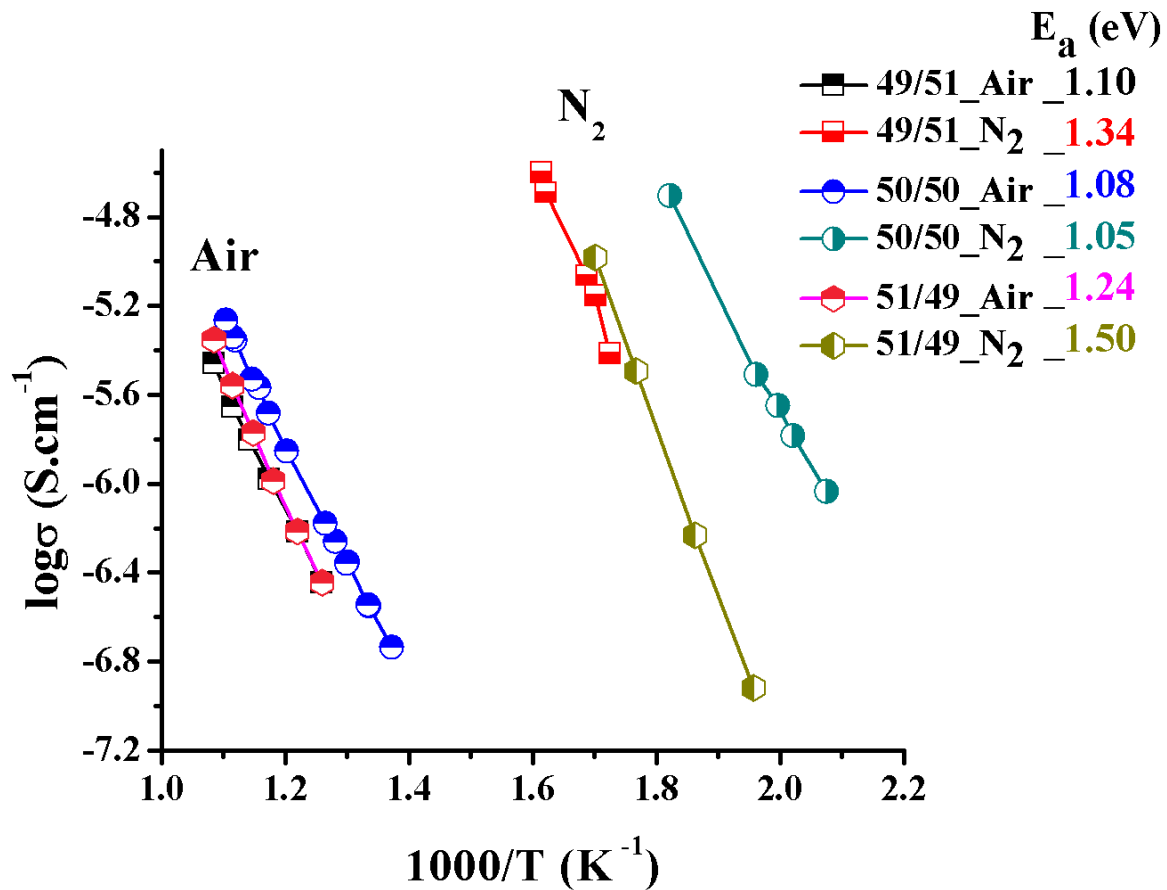


Figure 8. Arrhenius plots of various air and N_2 sintered KNN from Impedance Spectroscopy data, inset with activation energy of each ratio. **NB the numeric in the colour coded key denotes the K/Na ratio and N_2 or air the sintering atmosphere**

To further confirm the nature of the conduction in KNN, the Seebeck coefficient (S) was determined [14]. This technique allows comparatively easy differentiation of p and n type behaviour. S was measured for KNN samples sintered in air and inert conditions. Negative voltages were observed for all samples fired in N_2 irrespective of composition confirming them to be n-type but in contrast, positive coefficients and therefore p-type behaviour was observed for all air sintered samples, as shown in Figure 9(a-e), where Figure 9(a-b) are plotted from heating data of bar samples and Figure 9(c-e) from furnace-cooling data. The lowest S values

were observed at T_{T-C} in agreement with Lee et al. (2009) in their investigation of the phase transitions in BaTiO_3 [15]. The cooling data in Figure 9(c) and (e) for air sintered samples KNN-50/50 and KNN-51/49, respectively clearly illustrate this trend. It should be noted however that the temperatures from the Seebeck measurements represent an average temperature across the sample **due to the thermal gradient across the bar sample** and thus are not exactly the same as those shown in Figure 3. Nonetheless, lower S values are consistently observed at the transition temperatures. We also note that heating cycles for air-fired samples showed consistent data but N_2 sintered samples revealed changes in the Seebeck coefficient depending on the number of cycles, albeit always n-type. Since the thermopower measurements were carried out in air, the elevated temperatures affect the V_{O}^{2+} concentration in N_2 -sintered samples. To test this hypothesis, KNN-50/50- N_2 was heated up to 600°C and cooled to room temperature three times in air, with the Seebeck data collected and plotted in Figure 9(d). The n-type behaviour associated with sintering in N_2 gradually changes to p-type as the number of heating/cooling cycles increases in air.

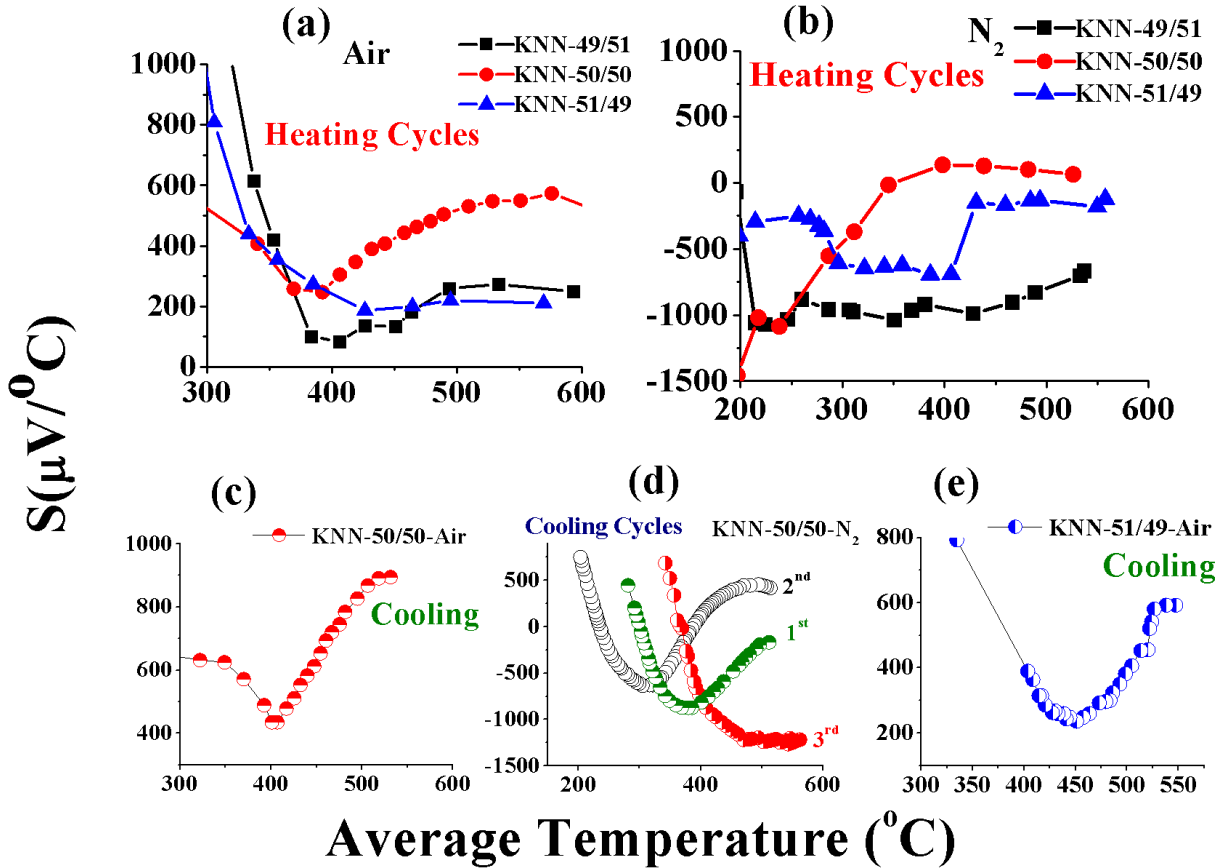


Figure 9. p-type vs. n-type behaviour of KNN 50/50 in the form of (top) positive Seebeck coefficient and (bottom) negative Seebeck vs. average temperatures range 300 to 550 °C, obtained on cooling.

Figure 10 shows the polarisation vs. field loops for air and N₂ sintered samples with ferroelectric properties tabulated in Table 1. The remanent polarisation (P_r) is higher in air-sintered samples except for KNN49/51 for which N₂ sintering gives higher P_r and P_{sat}, consistent with enhanced piezoelectric properties, Figure 11. In K-rich samples, there is only a slight difference between P_r and the saturation polarisation (P_{sat}) which suggests the leakage current for both compositions is low, consistent with the impedance spectroscopy data. In all samples, the coercive field (E_c) is higher in N₂ which suggests that N₂ increases the degree of difficulty of polarisation reversal,

consistent with the premise that $\text{Nb}_{\text{Nb}}^{\text{/}}-\text{V}_\text{O}^{\bullet\bullet}-\text{Nb}_{\text{Nb}}^{\text{/}}$ defect dipoles are present within the samples that pin domains[16, 17]. The preliminary piezoelectric data are shown in Figure 11. d_{33} and k_p values of KNN are higher in K-rich samples with respect to other compositions; most probably due to the grain size increase (Figure 2) [18, 19].

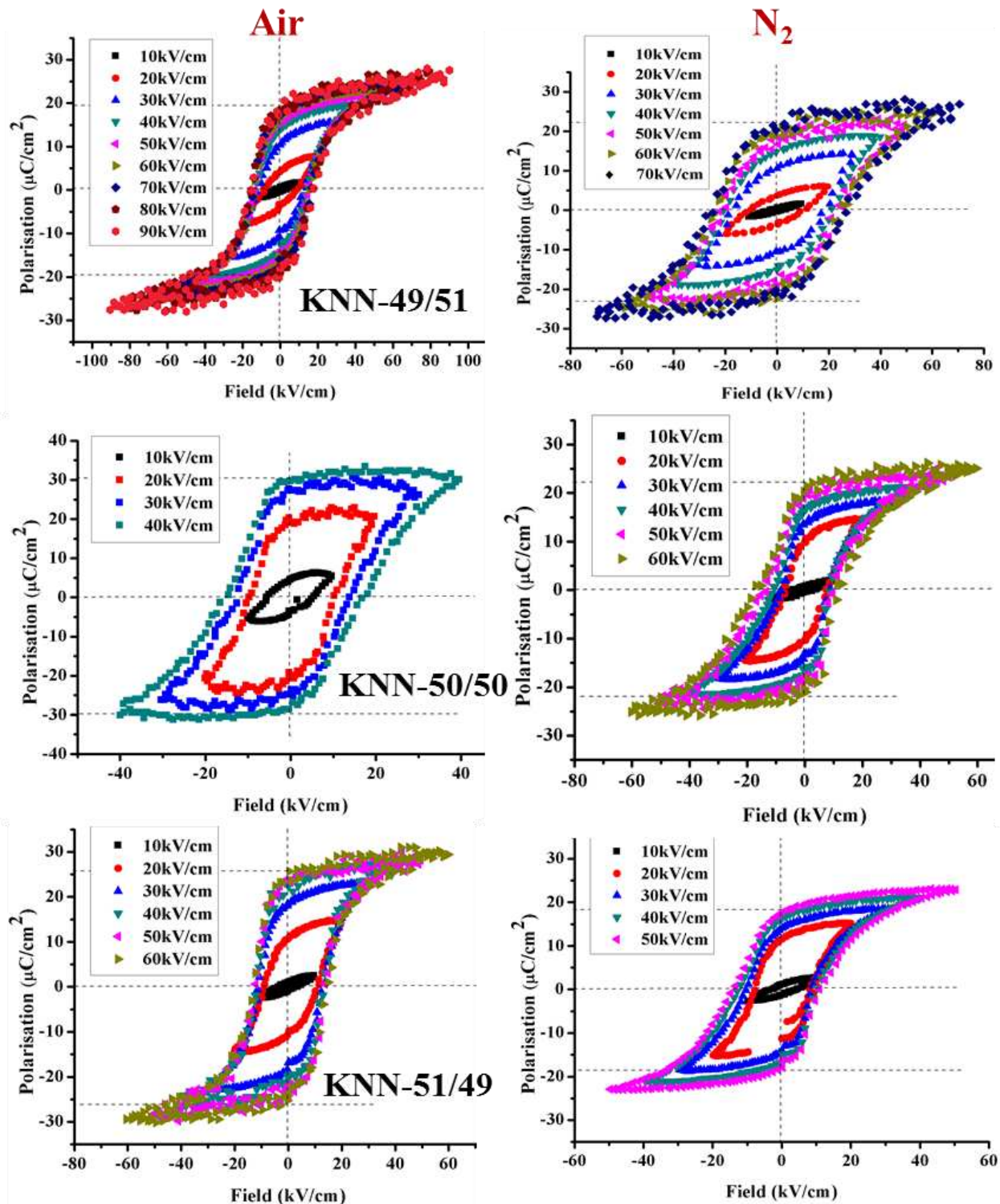


Figure 10. P-E hysteresis loops of air and N_2 sintered KNN samples.

Table 1. Key erroelectric values from Figure 10

Sample Name	P_r ($\mu\text{C}/\text{cm}^2$)	P_{sat} ($\mu\text{C}/\text{cm}^2$)	E_c (kV/cm)	Max. Applied Field (kV/cm)
KNN-49/51 Air	19	26	18	90
KNN-49/51 N ₂	20	27	26	70
KNN-50/50 Air	29	30	17	40
KNN-50/50 N ₂	21	25	18	60
KNN-51/49 Air	25	29	12	60
KNN-51/49 N ₂	18	23	13	50

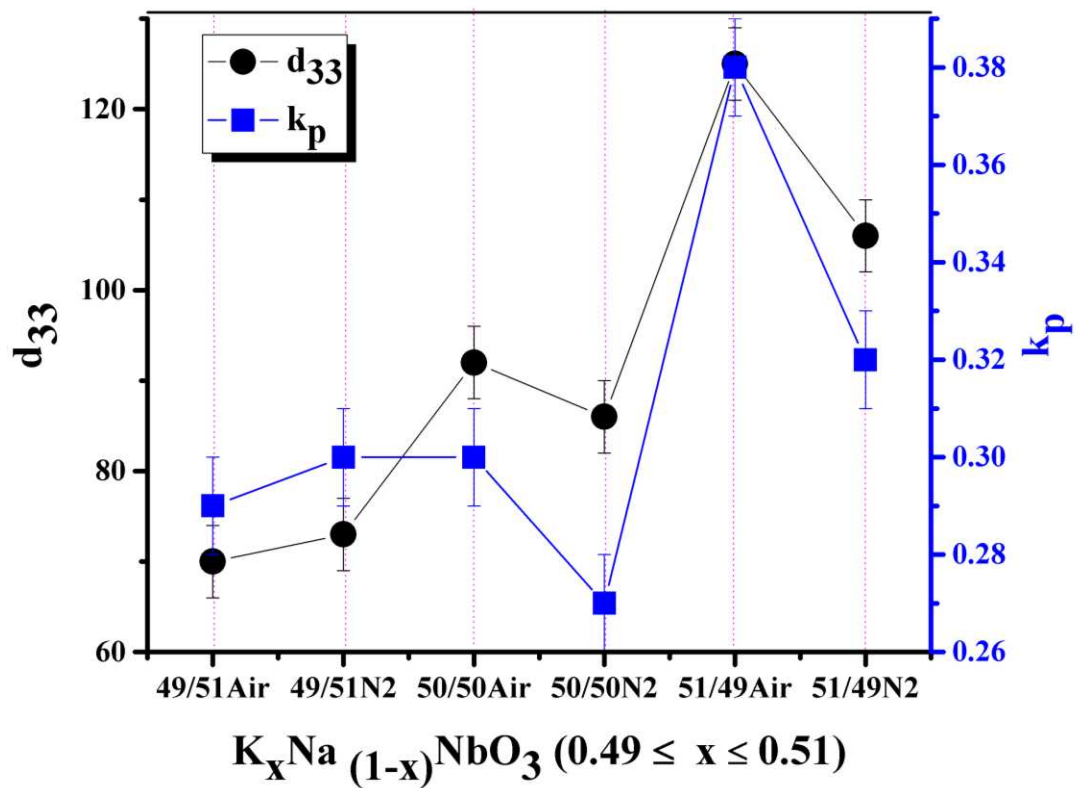


Figure 11. Piezoelectric properties of KNN compositions.

Many researchers have used CuO and/or MnO dopants in air processed KNN 50/50 and their results showed Cu²⁺ and Mn²⁺ substitute for Nb⁵⁺ as an acceptor (Mn/Cu^{III}_{Nb}). [20-25] In this case, V_O^{••} are created to maintain electroneutrality as in defect equation (1). [20-25] These vacancies and acceptor dopants are considered to create defect dipoles (Mn/Cu^{III}_{Nb} - V_O^{••}) providing a restoring-force that results in harder KNN ferroelectric and piezoelectric properties. The addition of CuO and MnO also results in an increase in conductivity consistent with the formation of V_O^{••}. We propose that reducing KNN effectively encourages a similar hardening effect due to the formation of Nb_{Nb}⁴⁺-V_O^{••}-Nb_{Nb}⁴⁺ rather than Mn/Cu^{III}_{Nb} - V_O^{••} defect dipoles.

Conclusions

Undoped KNN was synthesized with different ratios of K⁺ and Na⁺ and fired in air and N₂. 95% relative density was obtained in these systems in air and N₂ utilising a conventional mixed oxide route. XRD of all undoped KNN ceramics and powders revealed an orthorhombic crystal structure with Bmm2 symmetry. Minor peaks of a tetragonal tungsten bronze structured secondary-phase (TTB) were observed in air but not in N₂ sintered pellets. Impedance spectroscopy and thermo-power analysis confirmed that un-doped KNN was p- and n-type when sintered in air and N₂, respectively. Moreover, dielectric losses increased in N₂ sintering conditions, presumably due to the formation of oxygen vacancies and accompanying electrons. Optimum P_r, k_p and d₃₃ were obtained for air-sintered samples with P_r=29μC/cm² for KNN_50/50_and d₃₃=125pC/N and k_p=0.38 for KNN_51/49. Equivalent samples sintered in N₂ had lower values of P_r, k_p and d₃₃.

Acknowledgements

FH and AK acknowledge (NED University of Engineering and Technology) & (Abdul Wali Khan University Mardan) for funding support of faculty development programme respectively. All authors acknowledge financial support from the Sustainability and Substitution of Functional Materials and Devices EPSRC grant (EP/L017563/1).

References

1. Kawada, S., et al., (K_{0.5},Na_{0.5})NbO₃-Based Multilayer Piezoelectric Ceramics with Nickel Inner Electrodes. *Applied Physics Express*, 2009. **2**(11): p. 111401.
2. Ibn Mohammed, T. et al., Integrated hybrid life cycle assessment and supply chain environmental profile evaluations of lead-based (lead zirconate titanate) versus lead-free (potassium sodium niobate) piezoelectric ceramics, *Energy Environ. Sci.*, 2016, **9**, 3495-3520.
3. Wang Q., J.Y., Wu Zhang, et. al., Manufacture and Cytotoxicity of a Lead-free Piezoelectric ceramics as a bone substitute. *International Journal of Oral Science*, 2009. **1**(2): p. 99-104.
4. Jalalian A., G.A.M., Biocompatible ferroelectric (Na,K)NbO₃ nanofibers. *Applied Physics Letters*, 2012. **100**(1).
5. Fisher, J.G., et al., High-temperature X-ray diffraction and Raman spectroscopy study of (K_{0.5}Na_{0.5})NbO₃ ceramics sintered in oxidizing and reducing atmospheres. *Materials Chemistry and Physics*, 2010. **120**(2-3): p. 263-271.
6. Fisher, J.G., et al., Structural changes in potassium sodium niobate ceramics sintered in different atmospheres. *Journal of Alloys and Compounds*, 2009. **479**(1-2): p. 467-472.

7. K.H. Hardtl , R.W., Lowering the Curie temperature in reduced BaTiO₃. Solid State Communications, 1972. **10**: p. 153-157.
8. Glaister R M, K.H.F., An Investigation of the Cubic-Hexagonal Transition in Barium Titanate. Proceedings of Physical Society, 1960. **76**(5).
9. Kobayashi, K., et al., A Route Forwards to Narrow the Performance Gap between PZT and Lead-Free Piezoelectric Ceramic with Low Oxygen Partial Pressure Processed (Na_{0.5}K_{0.5})NbO₃. Journal of the American Ceramic Society, 2012. **95**(9): p. 2928-2933.
10. Tsai, C.-C., et al., Influence of A-site deficiency on oxygen-vacancy-related dielectric relaxation, electrical and temperature stability properties of CuO-doped NKN-based piezoelectric ceramics. Ceramics International, 2013. **39**: p. S165-S170.
11. Wang, K. and J.-F. Li, (K, Na)NbO₃-based lead-free piezoceramics: Phase transition, sintering and property enhancement. Journal of Advanced Ceramics, 2012. **1**(1): p. 24-37.
12. Eriksson, M., et al., Ferroelectric Domain Structures and Electrical Properties of Fine-Grained Lead-Free Sodium Potassium Niobate Ceramics. Journal of the American Ceramic Society, 2011. **94**(10): p. 3391-3396.
13. Irvine John T. S., Sinclair .D.C., West A. R., , Electroceramics: Characterisation by impedance sepctroscopy. Advanced Materials, 1990. **2**: p. 132-138.
14. Kasap, S.O., Thermoelectric effects in Metals: Thermocouples, 1997-2001: The department of Electrical Engineering, University of Saskatchewan Canada. p. 01-11.
15. Lee, S., et al., Thermopower in highly reduced n-type ferroelectric and related perovskite oxides and the role of heterogeneous nonstoichiometry. Physical Review B, 2009. **79**(13).

16. Wang, T., et al., Defect-driven evolution of piezoelectric and ferroelectric properties in CuSb₂O₆-doped K_{0.5}Na_{0.5}NbO₃ lead-free ceramics. *Journal of the American Ceramic Society*, 2017. **100**(12): p. 5610-5619.
17. Lv, J., X. Lou, and J. Wu, Defect dipole-induced poling characteristics and ferroelectricity of quenched bismuth ferrite-based ceramics. *Journal of Materials Chemistry C*, 2016. **4**(25): p. 6140-6151.
18. Xu, F., et al., Domain wall motion and its contribution to the dielectric and piezoelectric properties of lead zirconate titanate films. *Journal of Applied Physics*, 2001. **89**(2): p. 1336.
19. Randall, C.A., et al., Intrinsic and Extrinsic Size Effects in Fine-Grained Morphotropic-Phase-Boundary Lead Zirconate Titanate Ceramics. *Jounal of American Ceramic Society*, 1998. **81**(3): p. 677-88.
20. Ebru Mensur Alkoy, A.B.Y., Electrical properties and impedance spectroscopy of pure and copper-oxide-added potassium sodium niobate ceramics. *IEEE Transactions on Ultrasonics Ferroelectrics and Frequency Control*, 2012. **59**(10): p. 2121-2128.
21. Li, E., et al., Enhancement of Q(m), by co-doping of Li and Cu to potassium sodium niobate lead-free ceramics. *IEEE Transactions on Ultrasonics Ferroelectrics and Frequency Control*, 2008. **55**(5): p. 980-987.
22. Körbel, S. and C. Elsässer, Ab initio and atomistic study of ferroelectricity in copper-doped potassium niobate. *Physical Review B*, 2011. **84**(1).
23. Eichel, R.d.-A., et al., Interactions of defect complexes and domain walls in CuO-doped ferroelectric (K,Na)NbO₃. *Applied Physics Letters*, 2013. **102**(24): p. 242908.

24. Alkoy, E.M. and M. Papila, Microstructural features and electrical properties of copper oxide added potassium sodium niobate ceramics. *Ceramics International*, 2010. **36**(6): p. 1921-1927.
25. Azough, F., et al., Microstructure and piezoelectric properties of CuO added (K, Na, Li)NbO₃ lead-free piezoelectric ceramics. *Journal of the European Ceramic Society*, 2011. **31**(4): p. 569-576.